Upper mantle structure beneath the eastern Pacific Ocean ridges

Yu J. Gu
Department of Physics, University of Alberta, Edmonton, Alberta, Canada

Spahr C. Webb, Arthur Lerner-Lam, and James B. Gaherty
Lamont-Doherty Earth Observatory, Columbia University, Palisades, New York, USA

Received 11 August 2004; revised 19 February 2005; accepted 14 March 2005; published 11 June 2005.

[1] We analyze vertical component body and surface waves for 10 $M_w > 5$ earthquakes, recorded by ocean bottom seismometers at regional and teleseismic distances. Through waveform modeling, we place new constraints on along-axis variation in temperature and partial melt beneath the eastern Pacific ridges. The resulting best fit models show over 9% variation in average lithosphere shear velocities between different ridge segments. We demonstrate that lid velocity correlates with the square root of plate age, consistent with a conductive cooling process, but we find a more rapid dependence on age close to the rise axis. We map the average plate age into a mean lithospheric temperature for each of our profiles using a half-space cooling model, and the temperature derivatives (dVs/dT) determined from least squares linear fits are -1.1 and -0.26 m s^{-1} deg^{-1}, respectively, for temperatures above and below $\sim$1000°C. The former estimate is more negative than values determined by earlier reports (-0.4 to -0.7 m s^{-1} deg^{-1}), using global or regional data from a much wider range of seafloor age but with less resolution at young ages. The high $|dVs/dT|$ value may suggest the presence of limited partial melt at shallow mantle depths, even after accounting for the strong effect of anelasticity and anharmonicity resulting from temperature and grain size variations. Our data also show a strong north-south difference in mantle structure: the surface waves that traverse the southern East Pacific Rise (EPR) experience shear velocities as low as $\sim$3.75 km s^{-1}, more than 0.2 km s^{-1} slower than the average mantle structure at comparable depths beneath the northern EPR and the Galapagos spreading center. This difference cannot be explained by the simple conductive cooling process or spreading rate variations between ridge segments. The slow seismic speeds in the low-velocity zone (LVZ) appear to require partial melt. The velocity difference might be solely caused by higher temperatures under the southern EPR, but it may also suggest more melt in the LVZ beneath the southern ridge axis due to potential differences in melt production or extraction compared to the north. In addition, differences in width or symmetry of the partial melt zones can affect the observed path-averaged velocities beneath these two segments. Finally, we determine more accurate depths for ocean transform earthquakes by analyzing the amplitude ratios between body and surface waves. The depths of these transform earthquakes are consistent with brittle deformation within the oceanic crust.

Citation: Gu, Y. J., S. C. Webb, A. Lerner-Lam, and J. B. Gaherty (2005), Upper mantle structure beneath the eastern Pacific Ocean ridges, *J. Geophys. Res.*, *110*, B06305, doi:10.1029/2004JB003381.

1. Introduction

[2] Much of the discussion of mantle structure and dynamics beneath ocean ridges has centered on how melt is transported from presumed, broadly distributed mantle source regions to focused zones near the ridge axis. Insight into these processes came both from direct observations or modeling of geochemical data, and from studies of seismic velocity and density of upper mantle material that indirectly constrain temperature and composition. From a seismological perspective, the eastern Pacific ridge system maintains the fastest seafloor spreading rate on Earth and provides the best natural laboratory for studying mantle melting. Recent discussions of structure and dynamics beneath the East Pacific Rise (EPR) have been greatly facilitated by regional and teleseismic earthquake data recorded by arrays of ocean bottom seismometers (OBS). In particular, near 17°S along the EPR, the 1995–1996 Mantle Electromagnetic and Tomography (MELT) experiment [*MELT Seismic Team*, 1998] provided evidence of low shear velocities [*Forsyth et al.*, 1998], anisotropy [*Wolfe and Solomon*, 1998] and a

0148-0227/05/2004JB003381$09.00

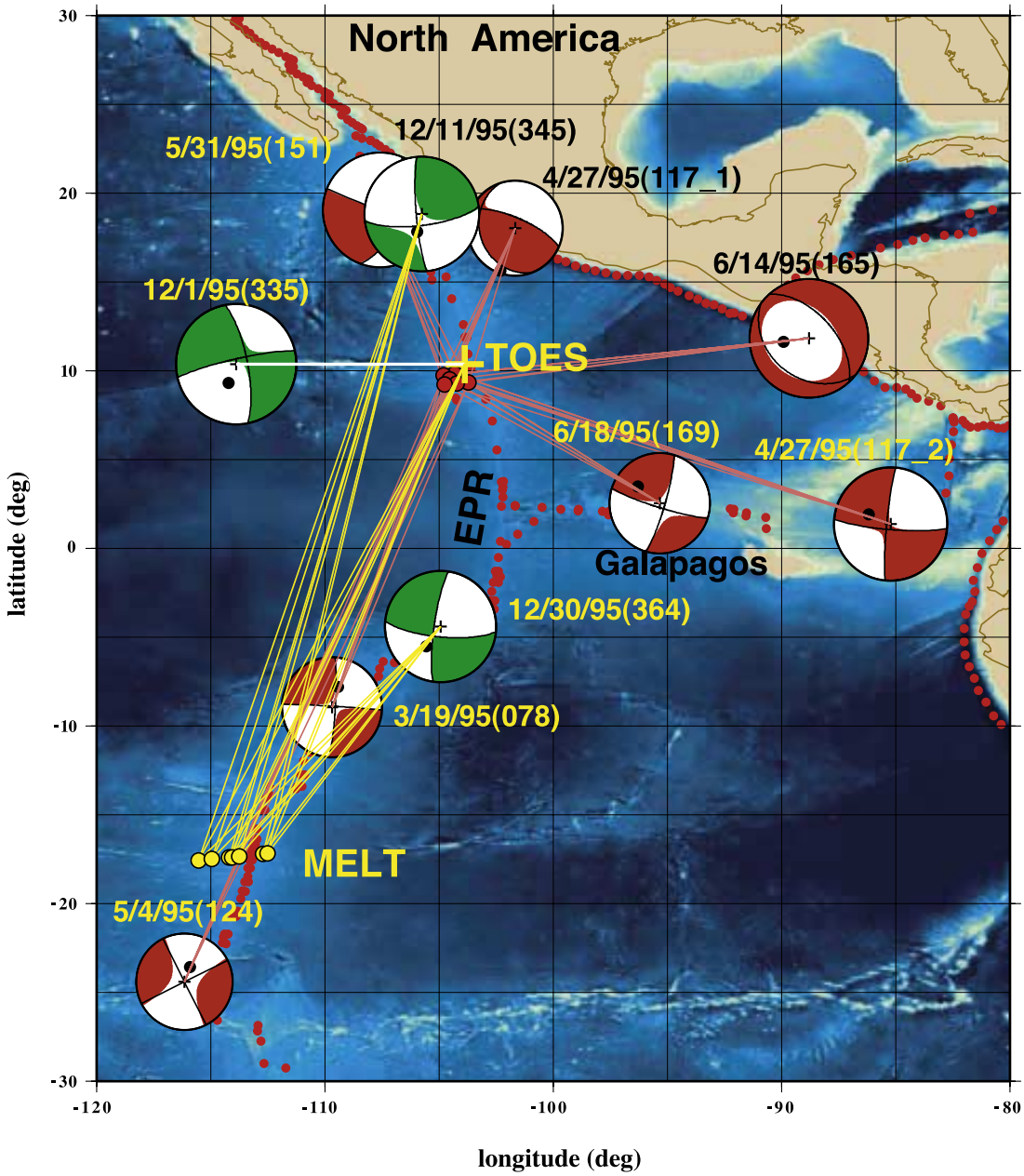

Figure 1. Bathymetric map showing the earthquake and station (OBS array) locations in the eastern Pacific. The source mechanisms are provided by the Harvard centroid moment tensor project. The green "beach balls" represent earthquakes recorded by the MELT array (yellow circles), and the remaining ones were recorded by the TOES array (red circles). These 10 earthquakes provide first-order constraints on the mantle structure beneath the different segments of EPR as well as the Galapagos spreading center.

strong east-west asymmetry in the shallow mantle [*Webb and Forsyth*, 1998; *Toomey et al.*, 1998; *Evans et al.*, 1999; *Dunn and Forsyth*, 2003] under this fast spreading ridge segment.

[3] The structures under the northern EPR and the Galapagos spreading center are less well studied. Regional [*Nishimura and Forsyth*, 1989] and global [e.g., *Su et al.*, 1994; *Li and Romanowicz*, 1996; *Shapiro and Ritzwoller*, 2002] studies reported low shear velocities in the upper mantle beneath this part of the ridge system. These studies relied on on-land recordings and have lateral resolutions on the order of 2000 km. Without projects like MELT and the order of magnitude resolution improvements made possible by OBS deployments, the connection between seafloor-spreading dynamics and mantle melting, particularly beneath the northern part of the eastern Pacific ridge system, remains weakly resolved.

[4] In this study we analyze the data from a small-scale OBS experiment conducted near 9°50′N along the EPR called Temporal Observation of Eruption Seismicity (TOES, 1995). This experiment produced regional data that constrain not only the ridge segments beneath northern EPR and the Galapagos spreading center, but also the southern EPR and allows for a convenient reappraisal of the structure

Table 1. Earthquake and Station Information

Day	Centroid Time, UT	Array	Latitude, °N	Longitude, °E	M_w	CMT Depth, km	Distance Range, km
95/078	1559:23	TOES	−8.94	−109.69	5.5	15.0	2080–2157
95/117_1	0642:22	TOES	18.04	−101.66	5.2	41.6	951–1029
95/117_2	1244:47	TOES	1.38	−85.23	6.2	15.0	2224–2353
95/124	2122:05	TOES	−24.41	−116.15	5.3	15.0	3919–3997
95/151	1608:42	TOES	19.05	−107.57	6.3	18.0	1070–1152
95/165	1111:56	TOES	11.82	−88.81	6.5	15.0	1651–1766
95/169	0342:16	TOES	2.54	−95.33	5.5	15.0	1191–1315
95/335	0520:36	MELT	10.38	−103.88	6.6	15.0	3188–3342
95/345	1409:26	MELT	18.84	−105.75	6.3	15.0	4047–4162
95/364	0326:18	MELT	−4.41	−104.94	6.1	15.0	1413–1606

obtained from the MELT experiment. This OBS data set depends primarily on ocean transform earthquakes and is only weakly affected by complexities associated with the crust and mantle structure beneath continental regions. We report here the first systematic analysis of the intermediate- and long-period surface wave data from this data set.

[5] Our approach is to determine shear velocity as a function of depth for the upper mantle beneath the ridges. By combining the TOES and MELT data sets, we explore the structural variations among different ridge segments beneath the eastern Pacific. The goal is to understand the relationship between shear velocity and seafloor age, and place it in the broader scope of lithosphere cooling and mantle melting. Our results demonstrate a linear relationship between lithosphere (lid) velocity and temperature after accounting for the effect of attenuation. Our analysis of the upper mantle low-velocity zone (LVZ) shows systematic differences between the northern and the southern EPR. These results will be examined in the context of melt generation and transport beneath ridge systems in general.

2. Data and Methods

2.1. Data

[6] In this study we combine the recordings of three transform earthquakes from the MELT experiment with seven $M_w > 5.2$ earthquakes from the TOES experiment (see Table 1). The study region and the source-station locations are shown in Figure 1. All selected events are found in the Harvard centroid moment tensor (CMT) catalogue, and the availability of source mechanism solutions (see Figure 1) greatly facilitates our analysis of seismic structure. The event-station paths from the TOES experiment provide the primary constraints on the mantle structure beneath the northern EPR and the Galapagos spreading center.

[7] Five ocean bottom seismometers (OBS) from the TOES experiment produce adequate signal-to-noise ratios (SNR) for both intermediate- and long-period records, especially on the vertical component that is least affected by tilt noise resulting from ocean currents. Figure 2 (top) shows an unfiltered vertical component trace for an M_w 6.5 earthquake, marked with distinctive *P*, *S*, and Rayleigh wave arrivals; arrivals beyond 400s are mostly caused by crustal and oceanic reverberations and the potential effects of multipathing. The filtered waveform in the passband [16s–33s] shows both *P* and Rayleigh waves, and the Rayleigh waves are also frequently detected above noise level in the longer-period range [50s–160s]. For the higher-frequency passband, the waveform enclosed in the phase window (shaded) is mostly sensitive to the upper 30–60 km (Figure 3, top). The longer-period data in the same time window provide additional constraints on the mantle structure between 80 km and 150 km (Figure 3, bottom).

2.2. Procedures and Starting Models

[8] In this study we mainly focus on Rayleigh waves and *S* phases that are polarized in the *P-SV* plane on vertical component records. All 10 events produce clear signals in the passband [16s–33s], and five have adequate SNR in the passband [50s–160s]. Synthetic seismograms are computed for laterally homogeneous, layered models with a reflectivity approach [*Fuchs and Müller*, 1971; *Kind*, 1978; *Herrmann and Wang*, 1985] that incorporates a water layer [*Xu and Wiens*, 1997] and the OBS instrument responses. We have corrected a phase error in the OBS instrument response algorithm used previously [*Webb and Forsyth*, 1998].

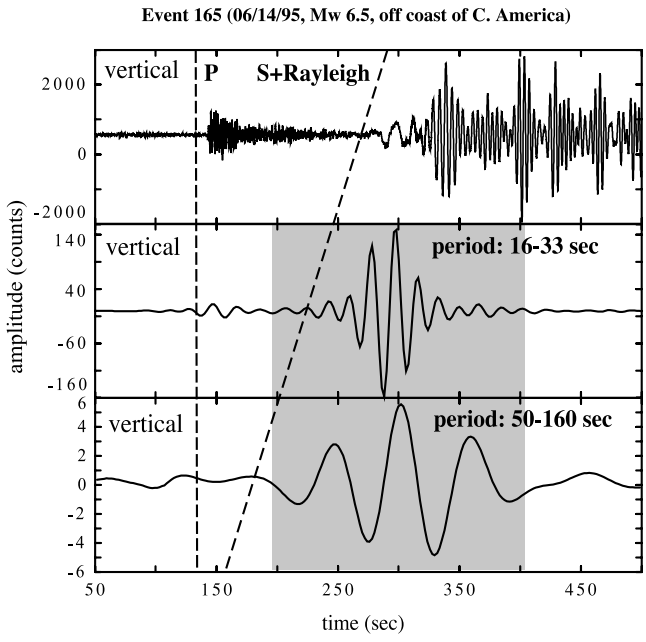

Figure 2. Sample waveforms on the vertical component. (top) An unfiltered trace with 32 Hz sampling, (middle and bottom) the filtered traces in period windows [16–33 s] and [50–160 s]. Clearly identified phases are *P*, *S*, and Rayleigh waves in the unfiltered trace; the longer periods are dominated by the Rayleigh wave energy (shaded window).

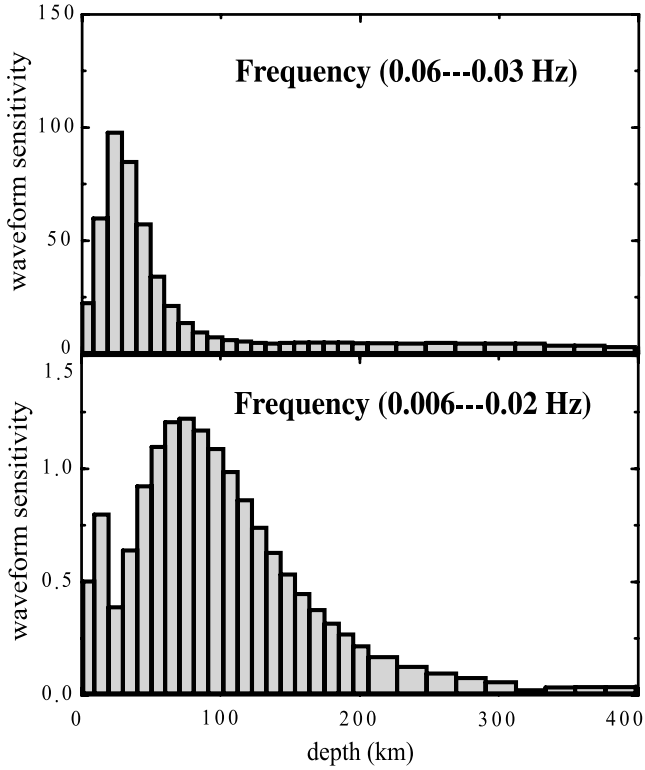

Figure 3. Depth sensitivity of *S* and Rayleigh wave window (shaded region in Figure 2) to a horizontally layered structure. The maximum sensitivities for period ranges [16–33 s] and [50–160 s] are observed at ~40 and ~90 km, respectively. The availability of the longer periods improves the constraint on the depth of LVZ.

[9] As the first step of the velocity analysis, we determine the compressional velocity by modeling the *P* wave arrival using a forward approach. The objective is to obtain a *P* wave structure accurate enough for the subsequent computation of Rayleigh wave synthetics. Most of our efforts, however, are focused on the shear velocities that have the dominant effect on surface waves. We adopt an iterative approach combining forward calculations (a user friendly java tool was developed to facilitate that undertaking) and linearized inversions [*Randall*, 1994] to achieve an optimal match between data and model synthetics for the time window containing *S* and Rayleigh waves. For both *P* and *S* velocity modeling we assume a density model that combines *Nishimura and Forsyth* [1989] (for the upper 300 km) and *Dziewonski and Anderson* [1981] (for the transition zone and lower mantle). The starting *Q* structures are modified from a model of Lau Basin [*Xu and Wiens*, 1997], a region of back arc spreading with a strong upper mantle low-velocity zone. We vary these *Q* models slightly to account for path age differences, though overall they have only minor effects on earthquake depth and shear velocity determinations.

2.3. Structure Above the Lid

[10] Potentially, lid velocity, crustal thickness, earthquake source parameters and ocean depth can all strongly affect the amplitudes and arrival times of Rayleigh wave waveforms (period > 15s), thereby influencing the determination of ocean mantle structure. In this study, however, path differences resulting from water depth and crustal thickness are small since our study area mostly consists of young oceanic lithosphere with nearly uniform crust (6–8 km) and known water depth. We use CRUST 2.0 [*Bassin et al.*, 2000] to fix the average crustal thickness and water depth along each source-receiver profile. CRUST 2.0 also provides the starting values for lid velocities, which are refined further by the iterative waveform inversion procedure. Also, prior to the inversions, records in the inversion time window are normalized to the peak amplitudes of Rayleigh waves to minimize the influence of instrument gain and seismic scalar moment.

2.4. Source Mechanisms and Depths of Earthquakes

[11] The source mechanisms used in our analysis are retrieved from the CMT catalogue. With $M_w > 5.2$, these earthquakes are generally well constrained from global body and surface waves. Most of the ocean transform earthquakes reside within 2–5 km horizontal distance from known fracture zones and the focal mechanisms generally reflect the expected local plate motions. The CMT source depths associated with these transform earthquakes (in most

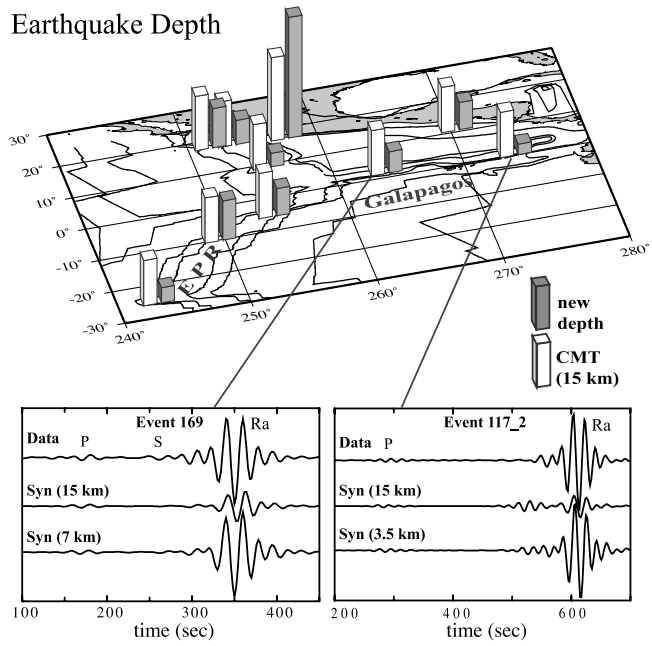

Figure 4. A comparison of CMT depths with depths determined from surface and body wave amplitudes by this study. The sample waveforms compare the observed (top traces) with synthetic seismograms computed using 15 km (middle) and the best estimates from this study (bottom). The CMT and final depths of the deepest event (117_1) are scaled by 0.67 for a better visual inspection. The assumed 15-km depth usually underpredicts the amplitude of surface waves, and more importantly, the ratio between body (*P*, *S*) and surface waves is nearly an order of magnitude smaller than the observed. The waveform amplitudes are greatly improved after relocating the earthquake depths to the final depths. All ocean transform earthquakes are moved to shallower depths.

Table 2. Depth and Scalar Moment Determination[a]

	Observed		CMT		Final Result				
Day	*P*/*Ra*	*S*/*Ra*	*P*/*Ra*	*S*/*Ra*	*P*/*Ra*	*S*/*Ra*	Depth, km	σ, km	Moment $M_0/M_{0\text{-CMT}}$
95/078	0.13	0.16	0.13	0.28	0.13	0.19	13.0	5.0	1.0
95/117_1	0.09	0.13	0.02	0.09	0.06	0.11	60.0	10.0	1.0
95/117_2	0.04	0.05	0.20	0.50	0.04	0.05	3.5	3.0	1.0
95/124	0.03	0.20	0.80	0.30	0.03	0.20	5.0	5.0	1.5
95/151	0.09	0.12	0.07	0.03	0.08	0.12	13.0	3.0	1.5
95/165	0.21	0.04	0.27	0.05	0.26	0.03	9.0	3.0	0.5
95/169	0.06	ND	0.12	ND	0.05	ND	7.0	3.0	1.0
95/335	0.03	0.05	0.08	0.50	0.03	0.10	4.5	3.0	0.5
95/345	0.06	0.10	0.20	0.06	0.13	0.08	8.0	5.0	0.7
95/364	0.07	0.20	0.14	0.02	0.02	0.20	9.0	5.0	0.8

[a]Determination of earthquake depth and scalar moment from the amplitude ratios of *P* wave versus Rayleigh wave (*P*/*Ra*) and *S* wave versus Rayleigh wave (*S*/*Ra*); σ represents the uncertainty in depth, and ND indicates that ratio cannot be determined.

cases, 15 km) are somewhat arbitrary and can be improved with our regional recordings. This is a critical step since the waveforms used in this study are strongly influenced by the earthquake depths (Figure 4). For two earthquakes near the Galapagos spreading center, the predicted Rayleigh wave amplitudes for the catalog source depth (15 km) are almost an order-of-magnitude smaller than the observed. This amplitude disparity cannot be explained by attenuation because realistic choices of attenuation parameters could only account for a fraction of the amplitude differences seen in these events. A more important consideration is the ratio between body (P, S) and surface wave amplitudes: the ratio of the predicted arrivals at 15-km depth is significantly smaller than that observed. By moving the earthquakes to the respective depths of 7 km and 3.5 km (slightly below seafloor), the overall amplitude and the ratio between body and surface waves become much more consistent with the observed (see Figure 4, bottom).

[12] The ratios between the observed, CMT and final depths are shown in Table 2. For each event we select the trace with the highest SNR to minimize the effect of multipathing, though for the most part the ratios are stable among the stations. The depth uncertainties (σ) are obtained based on the ratios as well as the SNR of the original data. The ratios computed from the final depths are greatly improved over CMT values, particularly for events 117_2, 151 and 165. The amplitude scaling factors between the data and final synthetics can be used to correct for the scalar moment M_0 in CMT solutions (see Table 1). We only provide rough estimates for M_0 because variations in *Q* and uncertainties in instrument gain could potentially cause significant changes in the absolute amplitudes of the synthetic seismograms. In comparison, earthquake depths are better constrained since relative amplitudes between body and surface waves are less sensitive to instrument gain.

[13] The best determined depths (relative to the ocean surface) of these 10 earthquakes are shown in Figure 4 (top). All of the ocean transform events included in this study are now shallower than 15 km and, with two exceptions, appear to reside within the oceanic crust assuming the crustal model of *Bassin et al.* [2000]. The relocated depths greatly enhance the compatibility of the OBS recordings and the synthetic seismograms computed from the starting one-dimensional (1-D) models. The empirical uncertainties (determined mostly from the quality of the records) are generally smaller than 3 km, especially for the ocean transform events (see Table 1), but the depths of two subduction zone earthquakes are less well constrained.

3. Model Results

3.1. Northern EPR (Above 9°50′N)

[14] The northern EPR is the most accessible fast spreading ridge to ships, and hence much of our understanding of ridge processes at fast spreading ridges has been derived from studies of this ridge. Spreading rates vary from 8 cm yr^{-1} in the north to about 13 cm yr^{-1} in the south near the Galapagos ridge-ridge-ridge triple junction. Several recent eruptions have been detected and intensively studied, as have their effects on the extensive hydrothermal biological communities found at vents along this segment. The 8–11°N segment is now a focus site for the RIDGE 2000 program involving integrated geochemical, geophysical and biological studies, and it continues to be a focus of active source seismic experiments [e.g., *Kent et al.*, 2000; *Canales et al.*, 2003].

[15] The 1995 TOES experiment (Figure 5a) offers unique regional earthquake data to complement such focused efforts. The ray paths from a Rivera Fracture Zone event (event 151) closely sample the Pacific side of the ridge axis, and the recordings from event 117_1 (Guerrero, Mexico) illuminate the ridge axis from the Cocos Plate side. An east-west comparison is of particular interest because a major ridge jump along the northern EPR within the last 2.5 Myr [*Lonsdale*, 1985, 1995; *Mammerickx et al.*, 1988] puts relatively old lithosphere close to western flank of the northern rise axis.

[16] Figures 5b–5d shows the fit of the synthetic waveforms to the observed vertical component seismograms for each station. Clear *P* and Rayleigh wave waveforms seen on the subduction zone event (117_1) are well predicted by the synthetics computed from a layered earth model. The model used for event 117_1 (Figure 6) is remarkably consistent with the 0–4 Myr ocean mantle model of *Nishimura and Forsyth* [1989] (hereinafter referred to as NF0-4), obtained using regionalized surface wave dispersion measurements for vast areas under the Pacific. The shear velocity under path 117_1 is characterized by a thin lid (10–20 km) on top

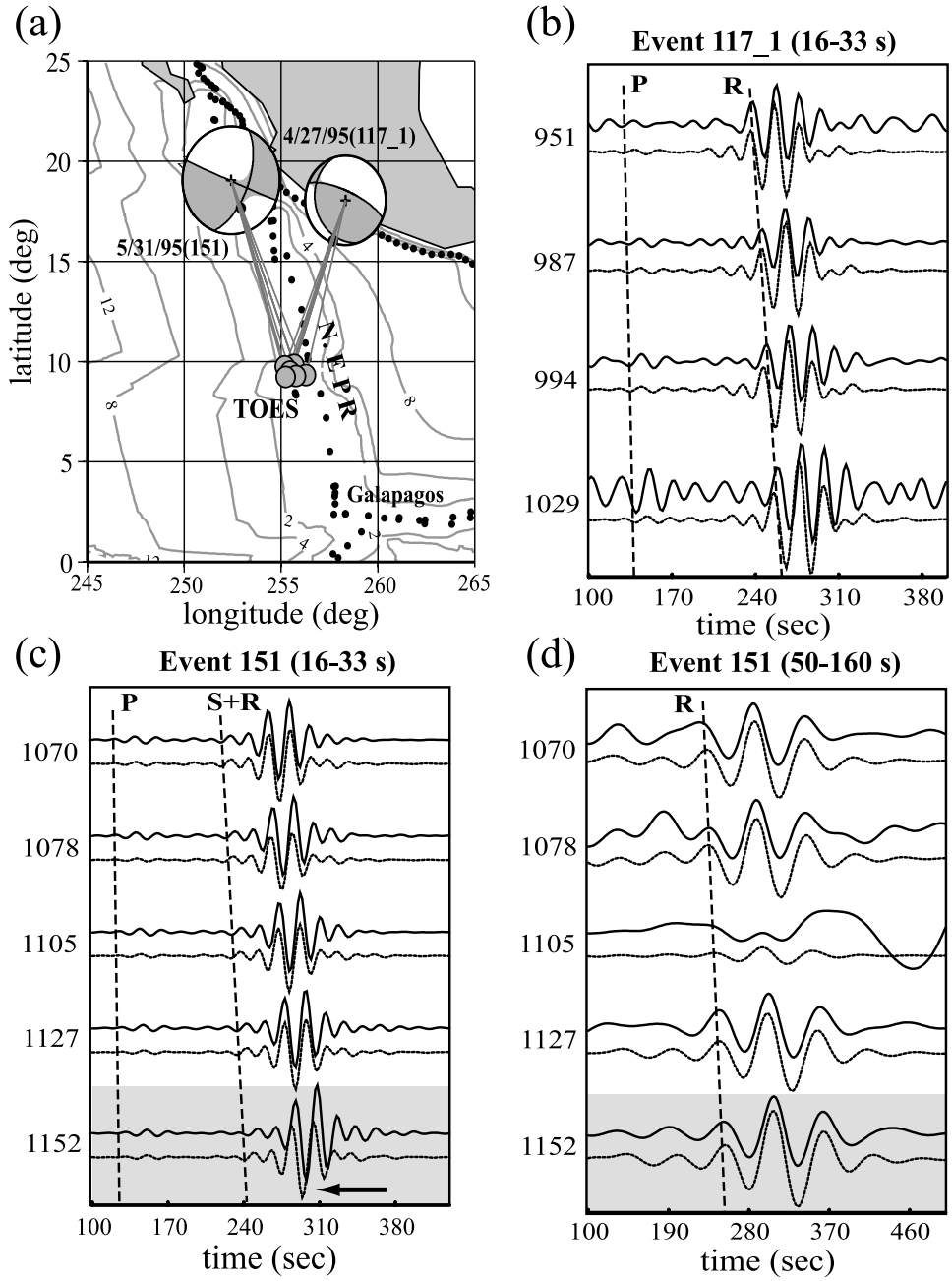

Figure 5. (a) Map showing the source and station locations of two events near the northern EPR. The background contour lines show a lithosphere age model in millions of years (Myr) [*Wessel and Smith*, 1991]. (b) Waveforms of four stations across the array (4 total, 1 with bad SNR) for event 117_1 and synthetics computed from the best fit model. The observed waveform at each station is the top trace in each set, and the model predictions are the bottom traces. The distance range (in km) between the source and station is shown for each trace. The *P*, *S* arrivals, and surface wave (R) are marked where evident. (c and d) Waveform fit to event 151, filtered at intermediate [16–33 s] and long [50–160 s] periods. The 1-D model obtained by this study explains the data well in both period ranges.

of a relatively steep negative velocity gradient that leads to the LVZ. The minimum velocity is ~4.1 km s^{-1}, comparable to NF0-4.

[17] The waveforms of event 151, the larger of the two earthquakes, can be modeled well at both intermediate (Figure 5c) and long (Figure 5d) periods. They require a model with a faster (4.5 km s^{-1} instead of 4.4 km s^{-1}) and thicker lid than that derived from event 117_1 (see Figure 6). Below 50 km, the LVZ is roughly 15 km deeper and 1% slower than the latter model. However, both models are substantially faster, in the top 100 km, than the Lau basin model of *Xu and Wiens* [1997] (hereinafter referred to as XW97), obtained from 1-D waveform modeling of surface waves.

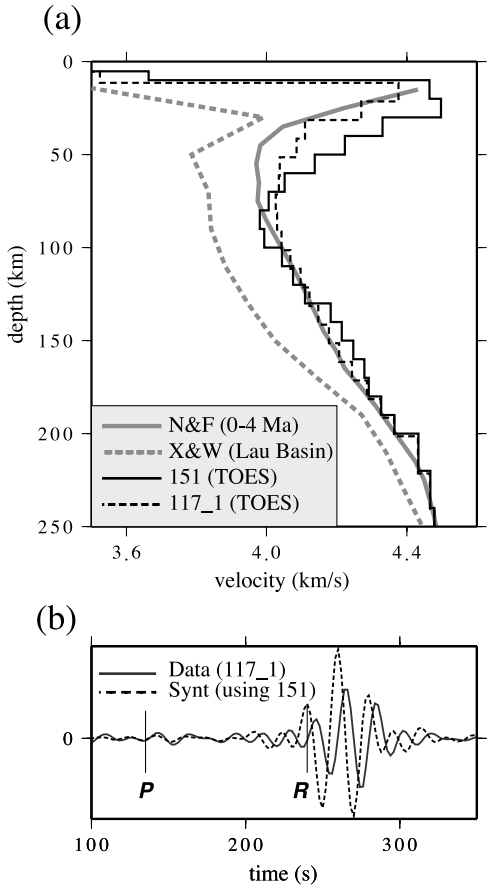

Figure 6. (a) Shear velocity with depth for the northern EPR. "N&F (0–4Ma)" represents the vertical shear wave speed of *Nishimura and Forsyth* [1989], determined for a 0–4 Myr oceanic mantle using surface wave dispersion measurements. "X&W" represents the Lau Basin shear velocity model of *Xu and Wiens* [1997] using a 1-D waveform inversion approach. The two models shown from this study differ in the top 30 km, due to differences in average crustal age, hence lid thickness, along the ray paths. The LVZ is similar but faster than that of NF0-4, and the corresponding velocities are significantly higher than those of X&W. (b) Fitting of a station record from event 117_1 using model 151 and showing path 151 is faster than path 117_1.

[18] The differences in lid velocity are adequately resolved. Using the velocity model from event 151 to generate waveforms for the event 117_1 data (or vice versa) produces both phase and amplitude errors (Figure 6b). The high lid velocity required by event 151 is characteristic of older oceanic lithosphere (>4 Ma) [e.g., *Nishimura and Forsyth*, 1989], which appears anomalous based on the path average age of 1.5 Ma we calculated from a global age model [*Mueller et al.*, 1997]. However, this global age model does not include the effects of a recent ridge jump of the northern EPR and therefore provides an erroneous estimate of average age along the ray path.

[19] Seafloor spreading on the EPR from the Rivera fracture zone (south to ~13°N) was originally focused on the Mathematician ridge until 3–7 Myr ago, when spreading jumped (through a process of ridge propagation, the formation of a microplate and eventual cessation of spreading on the western ridge) to its present position several hundred kilometers to the east. The old Mathematician paleoplate is evident in the magnetic anomaly stripes left on the seafloor [*Lonsdale*, 1985, 1995; *Mammerickx et al.*, 1988]. The seafloor age to the west of the present EPR increases from zero to roughly 3 Myr, and jumps beyond the Moctezuma trough region (the paleoplate boundary) to ages greater than 10 Myr [*Klitgord and Mammerickx*, 1982]. This old piece of oceanic crust between 13°N and the Rivera fracture zone raises the average age along the event 151 ray path to about 6 Myr, consistent with the thick lid in the model for this event (see Section 4). The ray path for event 117_1 to the east of the ridge axis crosses only young oceanic plate formed at the current EPR ridge axis.

3.2. Galapagos Rise Fracture Zone and Middle American Trench Events

[20] The ray paths from three TOES events, two on Galapagos Rise fracture zones and one in Middle American Trench, cover much of the Cocos plate (Figure 7). While they do not sample the ridges as effectively as those presented in sections 3.1 and 3.3 (see below), the wider span of crustal age beneath them enables a close examination of the effect of conductive cooling [*Turcotte and Oxburgh*, 1967] beneath this region. In particular, paths from events 169 and 117_2 are sensitive to the structures beneath both the Galapagos Spreading Center and the EPR. It should be noted also that although the Galapagos spreading center is strongly influenced by the nearby Galapagos hot spot, none of these ray paths directly samples the hot spot.

[21] Figure 7 shows the observed and synthetic traces for these three events. The average age under the source-receiver paths increases from ~2.4 Myr for event 169 to 9.0 Myr for event 165. Overall, the observed waveforms closely match the theoretical calculations, with relatively minor station-to-station variability.

[22] The lid velocity, which we loosely define as the average velocity from the Moho to the depth defined by the largest negative velocity gradient below the lid in each model, increases progressively as the rays move further away from the ridge axes (Figure 8). The lid beneath path 165 (9 Myr) is ~5% faster than path 117_2 (4.2 Myr), and over 8% faster than path 169 (2.4 Myr). Below the lid, differences in the models are small: all three paths require a distinct LVZ with a minimum velocity close to 4 km s^{-1}. The LVZ velocity is nearly identical to that in NF0-4 but significantly faster than XW97. Because the geometry of these source-receiver pairs are not strictly ridge parallel, the velocities extracted from these data represent path averages of oceanic mantle of different ages and of varying azimuth relative to the spreading direction. Azimuthal anisotropy could bias these velocity estimates by as much as 2% [*Forsyth et al.*, 1998; *Montagner*, 2002], particularly for events 169 and 165 that propagate along and perpendicular to the ridge axis of northern EPR and the Galapagos ridge. As spreading is occurring on both ridges, the direction associated with the fastest velocity may rotate along the ray paths for these events.

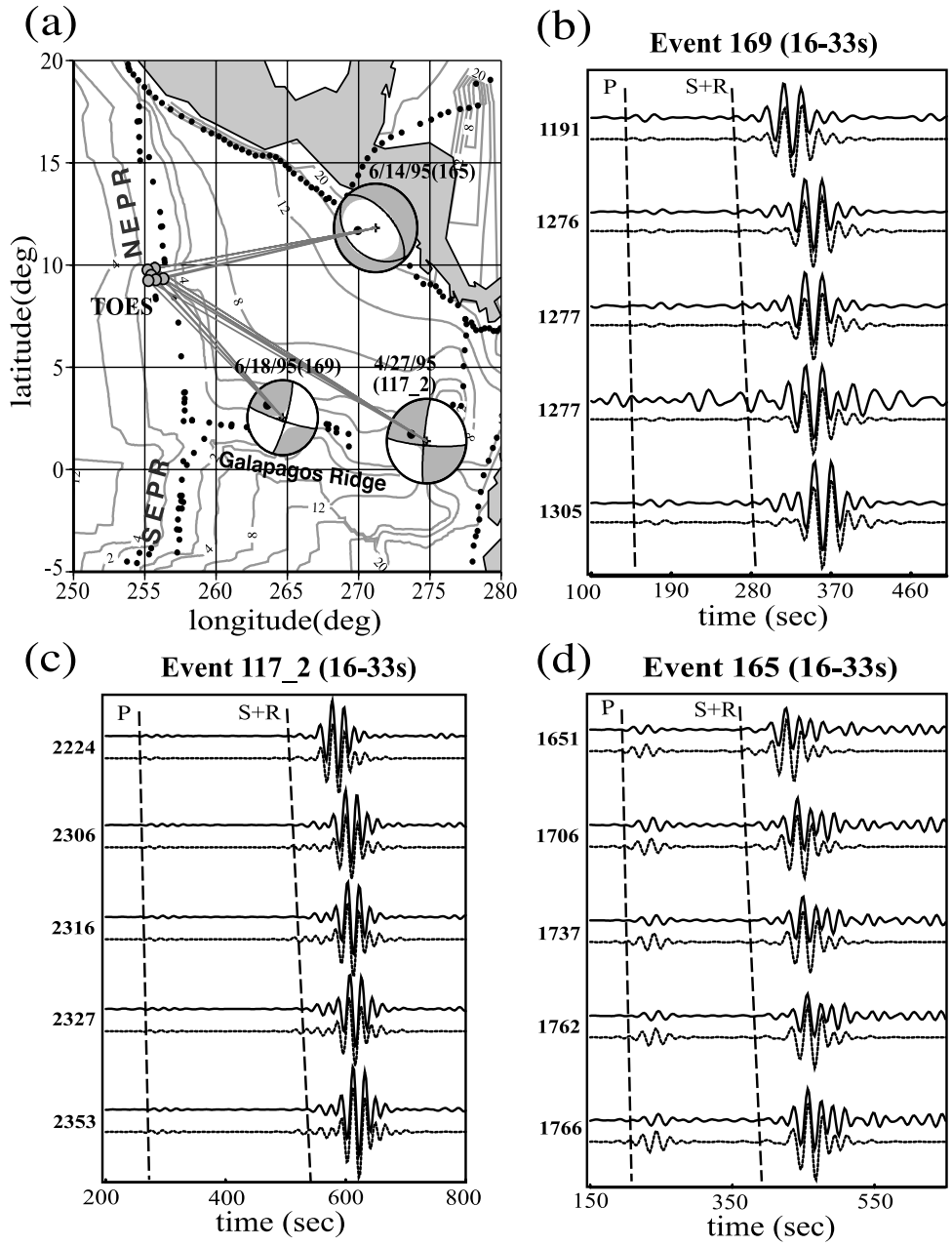

Figure 7. Locations and waveforms of three earthquakes that sample the Galapagos ridge and part of the northern EPR (see Figure 5 for shading conventions). (a) Event and station locations. The average path age increases rapidly from event 169 to 117_2 to 165 as they move away from the Galapagos ridge crest. (b–d) Observed and model predicted records for events 169, 117_2, and 165. All traces are filtered between 16 and 33 s. The long-period surface waves (not shown) are also explained by the best fit models.

[23] The observed progressive increase in lid velocity with age appears to be consistent with conductive cooling of oceanic lithosphere. Below 60 km, the similarity in the LVZ structures suggests relatively uniform thermal and melting conditions beneath the Cocos plate. We do not witness any definitive difference between a potentially hotspot-influenced mantle beneath path 117_2 and a normal "ridge mantle". Figure 9 shows the sensitivity of Rayleigh waveforms to the structure of the lid, using event 117_2 as an example. Models 1 and 2 (Figure 9b) have similar average velocities in the lid and therefore similar phase (Figure 9a), but model 2 with the slower, thicker lid fits the waveform much more accurately. By carefully matching the entire waveform, rather than selected portions of it, we obtain the most accurate structure among competing models. Conservative evaluations of errors in the resulting models range from ±0.03 to ±0.06 km s^{-1} in the top 100 km. These are only rough estimates: formal errors are difficult to

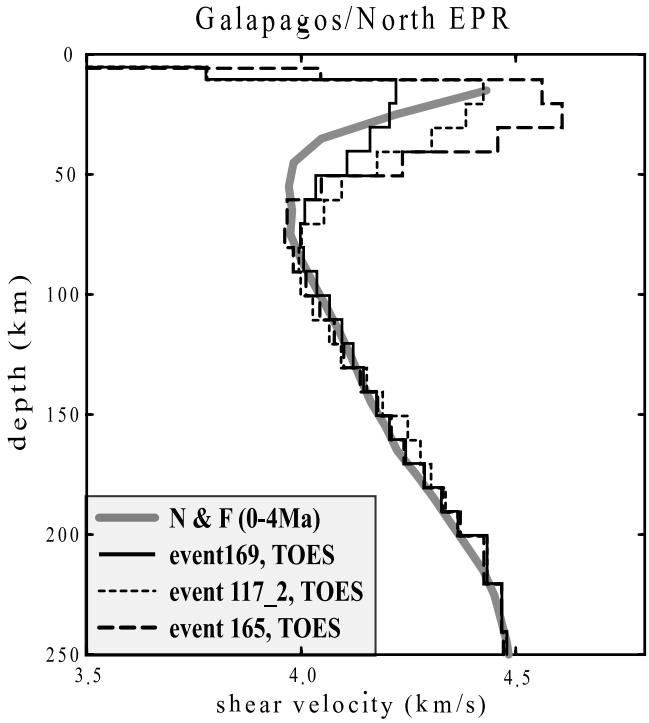

Figure 8. Model comparison between NF0-4 and those obtained from the three events shown in Figure 7. Models of this study show clear age dependence: events that are closer to the ridge, i.e., sampling a younger mantle regime, have slower velocities than those that are far from it. The LVZ is deeper and slightly faster than that predicted by NF0-4.

quantify because they depend not only on formal estimates derived from the inversions, but on factors such as event mislocation and the choice of model parameterization.

[24] As a simple test of our OBS data set, we compare the surface wave waveforms recorded by a GSN (on-land) station with that predicted by an OBS-based model (Figure 10). Because event 335 recorded by Global Seismic Network station JTS has nearly identical source-receiver path as those used to derive model 165 (see Figure 10a), we can directly evaluate this model using an independent, well-calibrated station. The predicted waveforms using model 165 (dotted) are generally consistent with the observed vertical component waveforms (black), particularly the Rayleigh waves which were modeled most effectively. The agreement between these two paths with opposite propagation directions suggests that nonspherical effects due to directional dependence, for example, possible dipping interfaces, are relatively small in the top 80 km of the upper mantle and confirms we have properly corrected for the OBS instrument response.

3.3. Southern EPR

[25] We combine the earthquakes from the MELT and the TOES arrays to analyze the mantle structure beneath the southern EPR (Figure 11). Ray paths resulting from events 078 (TOES), 335 (MELT) and 124 (TOES) have different lengths but similar azimuths that span most of the southern EPR. The overlap in path coverage allows for a reappraisal of existing models, as well as for differentiating the mantle structure beneath various segments along the north-south trending ridge. Generally, shear waves from the southern EPR are more difficult to model than those associated with the northern EPR and Galapagos spreading center. Within this subset of data, the waveforms of events 124 and 335 can be modeled fairly accurately (Figure 12), but the misfit between data and synthetics increases at sites further away from the rise axis. The wide aperture of the MELT array and potentially strong lateral velocity gradients are largely responsible for the observed interstation variability [e.g., *Dunn and Forsyth*, 2003], especially for event 335.

[26] The most distant event (345) shows clear evidence for lateral heterogeneities within the ridge mantle (Figure 13a). An increasing data synthetic misfit with east-west offset from the ridge correlates with the difference in ray length and ray geometry. We hypothesize that the lateral heterogeneity has led to a horizontal bending of the ray path, and a few (~3.5) degree change in the arrival angle of wave front at the MELT array. This causes the observed Rayleigh wave to arrive 10–15 s earlier than the

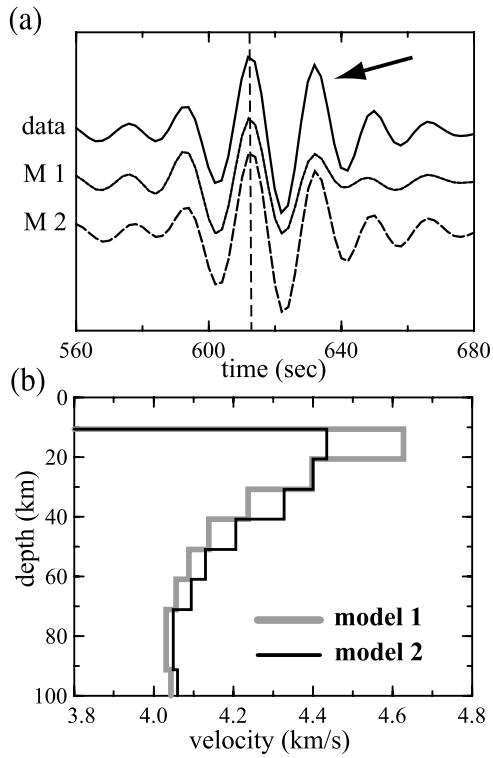

Figure 9. Waveform sensitivity to the LVZ and upper asthenospheric structure. (a) Top trace, a sample waveform from event 117_2. M1 and M2 show the waveforms produced by two competing models. Model 1 clearly explains the early part of the arrivals corresponding to surface waves with faster group velocities, but it fails to explain the latter part of the Rayleigh wave. Model 2 is the superior model that reproduces the entire wave train. (b) A comparison of the two competing models. Significant differences can be seen in the top 60 km of the structure between them, despite the seemingly small misfit shown in Figure 9a.

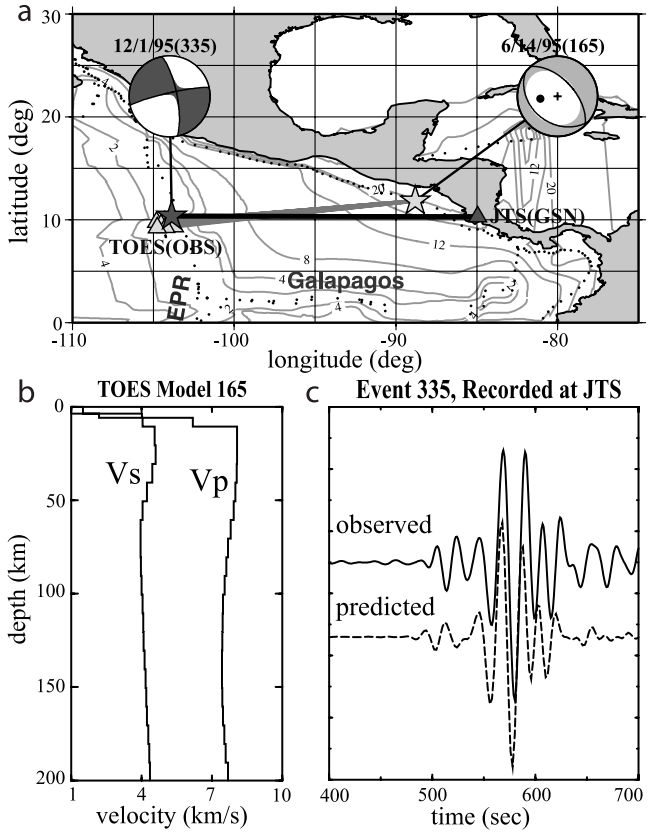

Figure 10. (a) Waveform fitting for data recorded at a GSN station (JTS) using the best fit model from event 165. (b) Near-overlapping paths that allow for a direct examination of the structure that we obtained from event 165, as recorded by the TOES OBS array. (c) Observed and predicted waveforms for event 335, recorded by an on-land station (JTS). The agreement between the waveform computed from model 165 and the observed record at JTS is remarkable, especially in the main Rayleigh wave arrivals, despite the differences in ray path, crustal structure, and wave propagation direction (opposite). This experiment demonstrates the robustness of our analysis and the consistency between OBS and on-land recordings.

model predictions at the longer paths (corresponding to the stations further to the west). Unlike the short-period data, the observed, longer passband Rayleigh waves do not show a substantial phase shift with respect to the synthetic waveforms across the ridge axis (Figure 13b). This could be a consequence of both lower SNR for the long-period data and, presumably, a weaker influence from lateral velocity variation at long wavelengths. Ray bending may be associated with the large region of anomalously slow LVZ velocities to the north and west of the MELT main array line as previously documented by *Forsyth et al.* [1998].

[27] Strictly speaking, the data from events 078 and 364 cannot be adequately explained by simple1-D models. Event 078 is a smaller magnitude earthquake with low SNR, while event 364 is close to the ridge axis and requires at least two to three models to fully capture the waveform variations across the array. The strong lateral variation in seismic velocities across the MELT array was previously documented by *Webb and Forsyth* [1998] and *Dunn and Forsyth* [2003]. We concentrate on the eastern part of the array for event 364, mainly to compare the resulting model with the structure of other parts of the EPR.

[28] All three models show a clear lid overlying the LVZ. Lid velocities range from 4.1 to 4.5 km s^{-1} and roughly correlate with the average path age (Figure 14). However, the lid velocity beneath path 335 is ~4% faster than that under path 124, despite their similar path age (3.3 and 2.9 Myr, respectively) and a substantial overlap in sampling over the entire distance between the TOES and MELT arrays. The only notable path difference is the extra 500 km of the ridge segment south of MELT (see Figure 11), traversed by path 124, which most likely result from anomalously slow velocities in this region. To examine the robustness of the aforementioned lid velocity difference, we comparing the waveforms of event 124 to synthetics calculated using the shear velocity structure obtained from event 335 (see Figure 14a, inset). The faster overall speed of the latter path translates into a 5-s earlier Rayleigh wave

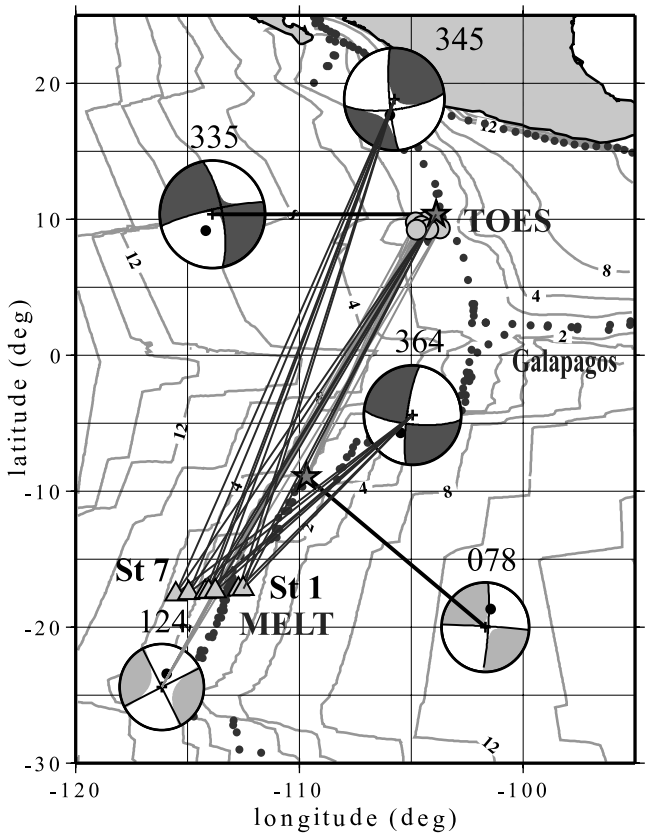

Figure 11. Map showing the ocean crustal age and earthquakes that sample the southern EPR. Stars mark the actual positions of event 335 and event 078, with the focal mechanisms removed for clarity. Events 078 (TOES), 124 (TOES), and 335 (MELT) have nearly overlapping paths, thus enabling a cross check of the models; model differences should reflect the different path lengths that sample the ridge axis of EPR. The ray path of event 364 is nearly fully embedded along the ridge, whereas event 345 only samples the southern EPR near the station sites.

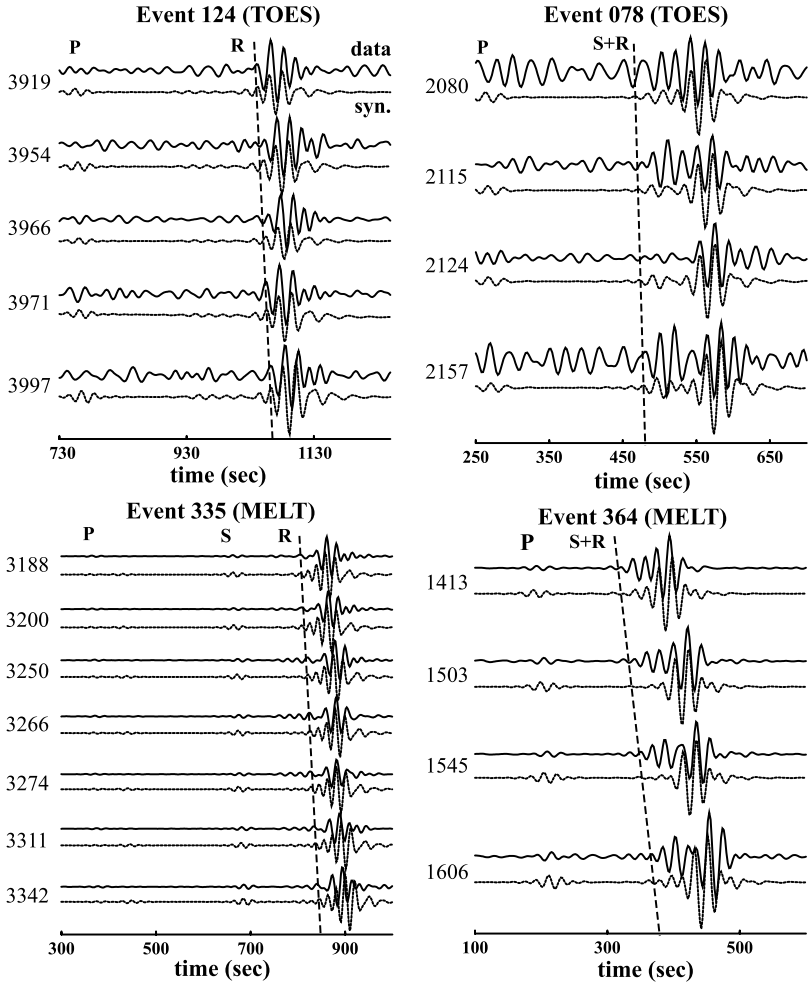

Figure 12. Data and synthetic seismograms associated with four events. A wider aperture array and greater 3-D effects associated with ridge mantle are mainly responsible for the markedly larger station-to-station variability relative to TOES. Events 124 and 335 are well modeled using our approach, despite a continuous phase shift between the data and the synthetic seismograms. Events 078 and 364 cannot be explained by simple 1-D models: the former is a smaller magnitude event with low SNR; the latter event requires at least 2–3 models to fully describe the variations across the stations [*Webb and Forsyth*, 1998].

arrival, but the wave shapes are well correlated because the lid models and their transitions to the LVZ beneath these two paths are otherwise similar.

[29] The source-station profile from event 078 overlaps with the northern half of the ray paths from events 335 and 124. The former averages to ~3.9 Myr, but the lid velocity beneath it falls between those of events 335 and 124 which is inconsistent with a simple conductive cooling model. The simplest explanation is that the ray trajectories deviate from the great circle path when traveling through high-velocity lithosphere and, consequently, the average age is underpredicted for the longer paths. The substantially shorter path from event 124 allows less ray bending away from the rise axis, hence requiring a slightly slower model relative to path 335.

[30] Beneath the lid, all three models show a pronounced LVZ, with the minimum shear velocity reaching as low as 3.8 km s^{-1}, which is considerably slower than the LVZ beneath the northern EPR. These values are all below NF0-4 between 30 and 60 km, and two of models have LVZ velocities comparable with XW97. The LVZ appears to terminate near 60 km, overlying a strong positive velocity gradient. Constrained mostly by the long-period waves, the robustness and nature of the positive gradient beneath the LVZ is still in question, though a sharp increase in shear velocities in the southern EPR has been supported by recent data and analyses from the GLIMPSE project [*Weeraratne et al.*, 2003]. If partial melt is responsible for a pronounced LVZ beneath the southern EPR, a strong positive velocity gradient beneath it would then mark the bottom of the melt zone in this region. The depth of the positive gradient is roughly consistent with the intersection of the dry solidus and a typical mantle adiabat in petrologic models of mid-ocean ridge melting [e.g., *Langmuir et al.*, 1992].

[31] For rays that travel along the axis of the southern EPR (event 364), the lid and LVZ velocities are by far the slowest among all the events of our study (see Figure 14b). The average lid velocity is more than 4% below that

obtained from event 124, the second slowest path, and the LVZ velocities are as low as 3.8 km s^{-1}. The latter velocity is about 0.25 km s^{-1} slower than NF0-4 and 0.1 km s^{-1} slower than XW97. The bottoming depth of the LVZ is not well constrained, though the long-period Rayleigh waves suggest a strong positive velocity gradient near 70–80 km depth. This estimate is only slightly deeper than other profiles of this study but 40–50 km shallower than those reported by *Webb and Forsyth* [1998]. In contrast, the velocity under path 345 (with average path age of 4.6 Myr) is considerably faster than NF0-4 in the upper 100 km, but it agrees well with *Nishimura and Forsyth*'s [1989] model for a 4–20 Myr ocean mantle. Only a modest LVZ exists along the path of event 345, which lies as much as 5 degrees away from the ridge axis.

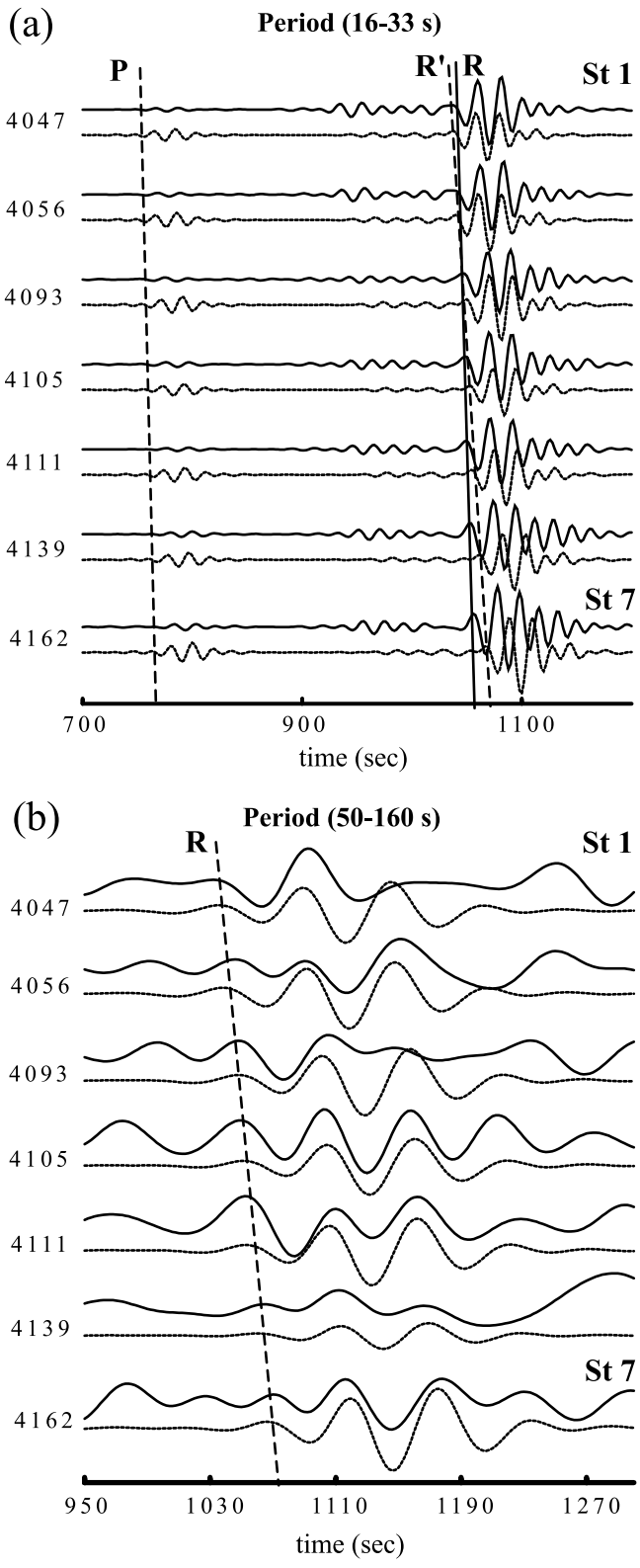

4. Discussion

[32] In view of plate tectonics, heat is lost from the Earth primarily through the creation and cooling of oceanic lithosphere as it moves away from mid-ocean ridges. On the basis of the simplest (half-space cooling) model, the heat flux out of the mantle is related to the square root of the age of oceanic crust and lithosphere [e.g., *Turcotte and Schubert*, 1982]. This relationship should be evident in the seismic velocities within the lithosphere, which are sensitive to lateral thermal, hence age, variations. By measuring seismic velocity as a function of lithosphere age, we can estimate the degree to which simple conductive cooling processes control velocity variations, and the degree to which melt, volatiles, and chemical variations are required [*Karato*, 1995; *Hirth and Kohlstedt*, 1996]. Our upper mantle models display strong variability in seismic velocities that appear to be a function of age, as well as of location along the ridge axis. To fully comprehend these results we place them in the context of lithospheric cooling and melting under ocean ridges.

4.1. Temperature Derivative and Lithospheric Cooling

[33] A simple linear scaling relationship between velocity and temperature has often been assumed when interpreting seismological models for geodynamic inferences. This assumption has been supported by the observed correlation between surface wave phase velocity and surface heat flow [e.g., *Nakanishi and Anderson*, 1984; *Nishimura and Forsyth*, 1989], although uncertainties in the scaling parameter remain relatively large, mainly due to the lack of depth resolution in seismological models and the potential presence of compositional variations, partial melt, and volatiles. The combined data from the MELT and TOES experiments place new constraints on the variations of velocity in the lithosphere with plate age. We obtain the mean lid velocity for each model by averaging the shear velocities in the depth range between the Moho and 40 km. We then assume a simple half-space cooling model [e.g., *Turcotte and Oxburgh*, 1967] to calculate the average lid temperature corresponding to the average seafloor age along each ray

Figure 13. Waveforms associated with event 345 at periods of (a) 16–33 and (b) 5–160 s. The solid travel time curve (labeled R) denotes the onset of observed Rayleigh wave arrivals, and the dashed curve R' shows the predicted arrival based on the model. A strong east-west difference arises because the stations in the east require rays to spend more time within the mantle melt zone. The path effect associated with mantle melt zone disappears at the longer periods (Figure 13b).

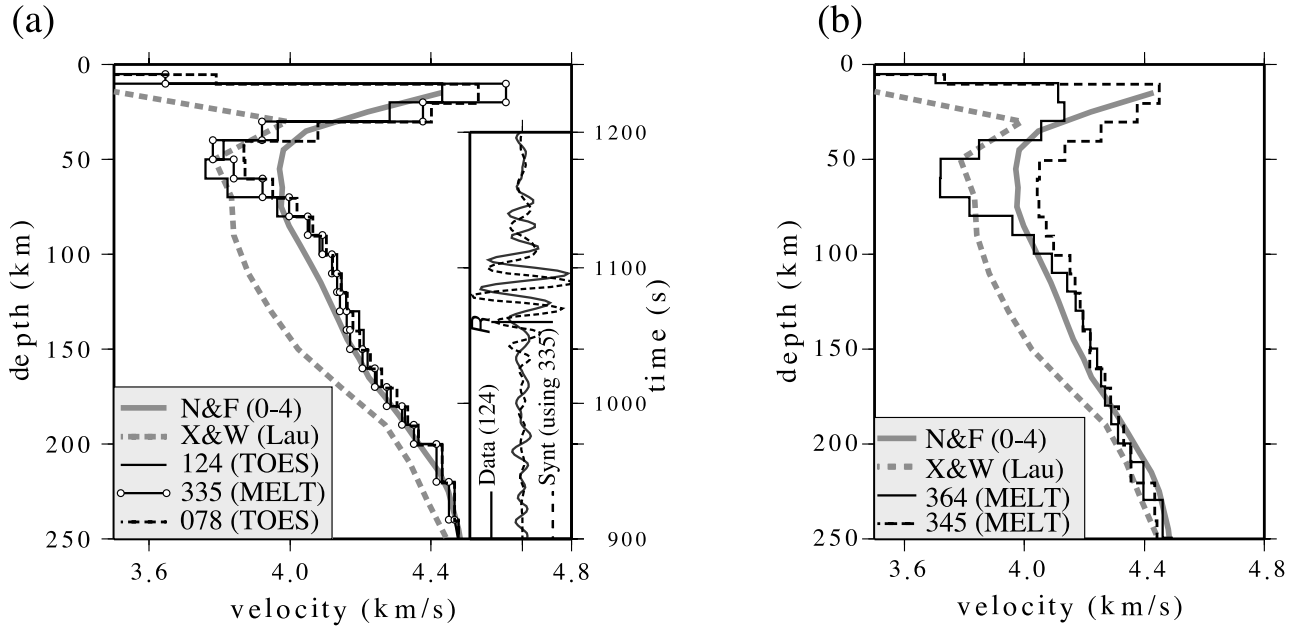

Figure 14. (a) Event 335, 078, and 124 model profiles. All three models, which are obtained from similar paths, contain a steep LVZ with velocities as low as 3.8 km/s. The LVZ appears to terminate at ~60 km, below which there is a strong positive velocity gradient. All three models are significantly slower than NF0-4 between 30 and 60 km and are comparable to the structure beneath Lau Basin at similar depths. The inserted waveforms show a record from event 124 (solid) and a waveform fit using model 335 (dashed). The differences in models 124 (slow) and 335 (fast) are required by the data. (b) Event 364 and 345 model profiles. The contrast between them, which shows a substantially faster mantle beneath path 345, illustrates the effect of conductive cooling of oceanic mantle away from the ridge axis. The model obtained from event 364 of this study is faster than the solution reported by *Webb and Forsyth* [1998] following a correction to the program.

path (Figure 15a). We use two ages for the ray path from event 151: the first (1.5 Myr) is calculated from the global age model of *Mueller et al.* [1997] which ignores the recent ridge jump associated with the Mathematician paleoplate, and a second corrected value (6 Myr) using age data for the paleoplate derived from *Mammerickx et al.* [1988].

[34] Figure 15b shows the resulting average lid velocity versus temperature for all the events analyzed by our study. We also include the average lid velocities for the V_{SV} models of *Nishimura and Forsyth* [1989] for lithosphere age groups 0–4,4–20, 20–52 and 52–110 Myr (represented by circles), obtained by the same approach as for our models. With the exception of paths associated with events 151 and 165 (with average path age of 6 and 9 Myr, respectively), most path ages from this study are younger than 5 Myr and the values cluster around NF0-4 on the temperature versus velocity plot. The data fall on two linear trends, one for age >5 Myr and another for the younger plate ages. If we group the corrected age value for path 151 with the older age data, the average lid velocity correlates linearly with temperature with a correlation coefficient $R = -0.97$ for path ages < 5 Myr, and $R = -0.93$ for path ages > 5 Myr, both of which are statistically significant.

[35] For a linear model the optimum regressions are -1.1 m s^{-1} deg^{-1} for the younger path ages, and -0.26 m s^{-1}deg^{-1} for the older path ages. These values provide estimates of the scaling between velocity and temperature (dVs/dT) which is, in a strict sense, a function of pressure averaged over the entire lithosphere. For ages less than 5 Myr, the absolute value of this temperature derivative is considerably larger than the previous estimates of 0.61 m s^{-1} deg^{-1} by *McNutt and Judge* [1990], obtained using global models of *Woodhouse and Dziewonski* [1984], 0.48 m s^{-1} deg^{-1} of *Kido and Seno* [1994], or 0.54 m s^{-1} deg^{-1} of *Kato* [1997] that was derived from the eastern Pacific anisotropic models of *Nishimura and Forsyth* [1989]. While these earlier values of dVs/dT were either based on global seismic data (first two studies) or regional data that span over 100 Myr in seafloor age (last study), our estimates reflect thermal signatures more spatially localized and the resolution at young oceanic crustal age is significantly higher than previous studies. For paths older than 5 Myr, the two data points from this study combined with NF4-20, NF20-52, and NF52-110 can be fit linearly (within the data uncertainty) with a dVs/dT value of -0.26 m s^{-1} deg^{-1}.

[36] The high $|dVs/dT|$ values in our study possibly suggest the presence of partial melt within the upper 40 km at seafloor ages <5 Myr, which would not only reduce *Vs* but also increase the temperature derivative of velocity [*Sato et al.*, 1989; *Kato*, 1997]. Solid-state effects can also increase $|dVs/dT|$, primarily through the dependence of shear velocity on anelasticity [*Karato*, 1993]. Anelastic or viscoelastic effects such as grain boundary

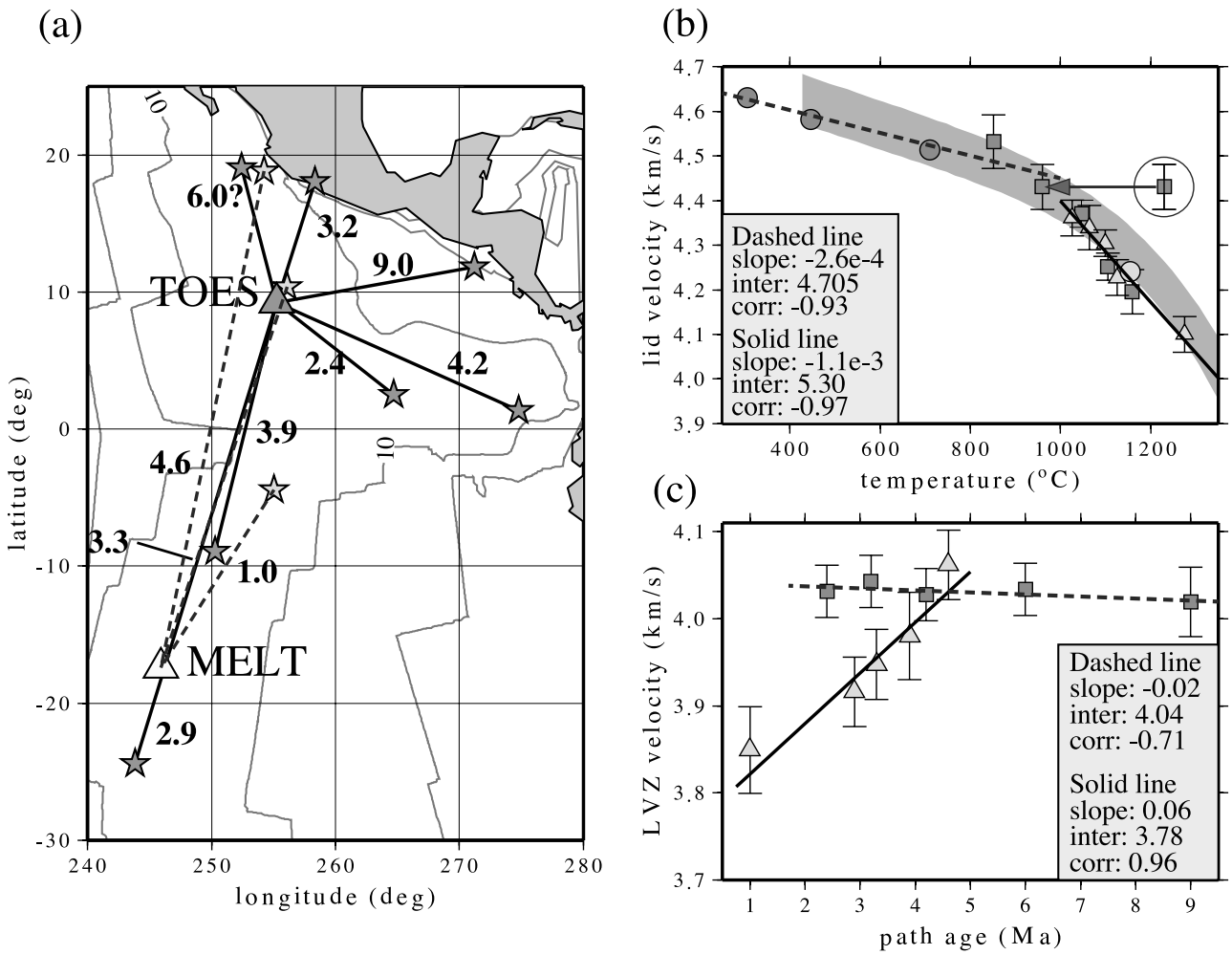

Figure 15. (a) Averaged ray path seafloor age computed using *Mueller et al.* [1997]. (b) Correlation of average lid velocity (see main text) with temperature. The initial event 151 age is shown circled before the correction for old oceanic crust associated with the Mathematician paleoplate. The values for paths traversing the southern EPR are represented by triangles, and the rest of the data from this study are represented by squares. Values for *Nishimura and Forsyth* [1989] are shown by circles, and the shadings distinguish ages older (dark gray) and younger (light gray) than 4.5 Myr. The solid line shows the least squares line fit to the corrected data values (including NF0-4) at temperatures above 1000°C. The thin dashed line shows a optimal line fit to the data (including those from *Nishimura and Forsyth* [1989] up to 110 Myr) at temperatures below 1000°C. The shaded curve on the background shows a range of nonlinear model predictions after accounting for anharmonicity and anelasticity [*Karato*, 1993; *Jackson et al.*, 2002] (see main text). (c) Average LVZ speed versus ocean age. We observe two distinct groups of values, those that correspond to southern EPR (triangle) and the rest (squares).

sliding induce nonlinear dissipation of seismic energy and changes in shear modulus (hence velocity), particularly at the high temperature range of 1000 to 1300°C [*Karato*, 1993; *Jackson et al.*, 1992, 2002]. To evaluate the solid state anelastic effects we compute the velocity versus temperature relationship using laboratory estimates of Q in olivine as a function of temperature [*Jackson et al.*, 2002], and then adopt *Karato*'s [1993] formulation of dVs/dT as a function of Q. We choose a period of 25 s, a grain size range of 0.5–1.0 cm, and assume a reference seismic velocity V_0 of 4.35–4.45 km s^{-1}, roughly consistent with the observed seismic speed for a 5-Myr lithosphere. All other parameters are fixed to values provided by *Jackson et al.* [2002] and *Karato* [1993]. The range of resulting nonlinear curves (see shaded curve in Figure 14b) roughly entails our observed values beneath young oceanic lithosphere, and conservatively, we conclude that our observations are consistent with solid-state cooling of an olivine-dominated mantle with moderate grain size. In detail, the overall trend of the data between 1 and 5 Myr appears to be explained better by a linear approximation and a steeper slope. This modest but visible departure of the observations from the nonlinear model may indicate the presence of partial melt within the upper 40 km of the mantle beneath seafloor

younger than ~5 Myr. That said, it is clear that the effect of frequency-dependent Q on the seismic velocities is important and a further analysis is underway.

[37] Away from the ridge axes, the low $|dVs/dT|$ value and the agreement with the nonlinear theoretical prediction both favor the absence of partial melt above 40-km depth. This conclusion is not critically dependent upon the choice of 40 km for an averaging depth for the lid, as we obtained the same result with averaging depths of 30 km, 50 km, or the depth of the steepest negative velocity gradient for each model [e.g., *van der Lee*, 2002]. We see the same value of dVs/dT required by the data points from north and south EPR alike (see Figure 15), which suggests that if partial melt is present, it should be uniformly distributed above the 40-km depth out to 5 Myr seafloor everywhere along the EPR. Significant partial melt in the mantle extending out to 4–6 Myr ages implies a melt zone of approximately 350 km (0.07m yr^{-1} × 3 Myr) wide in this region, which is roughly consistent with observations from the MELT experiment [*MELT Seismic Team*, 1998]. Alternatively, it is possible that the enhanced value of dVs/dT at young ages is simply a geometrical effect that arises from the combination of our limited path coverage and a localized near-axis melt zone. Because both arrays are located on axis, all of the paths directly sample the near-axis region. By definition, paths with younger average ages spend a greater percentage of their propagation time near the axis, and thus the impact of a localized melt zone is proportionally greater at younger ages than at older ages. We feel that this scenario is not likely, as it predicts that mean velocity would change linearly with mean path age, which we do not observe.

4.2. Low-Velocity Zone

[38] We investigate the potential correlation between the age of the oceanic lithosphere (i.e., proximity to the ridge axis) and the structure within the underlying LVZ (Figure 15c). The average LVZ velocity is obtained by averaging the velocities between the bottoming layer of the lid (the depth of the maximum negative gradient) and 100-km depth. These are empirical estimates aimed at understanding the similarities and differences between the ridge segments. Because the LVZ is below the lithosphere and therefore, by definition, minimally influenced by plate cooling, we do not have a theoretical model that predicts the velocity dependence on age. However, earlier modeling results have suggested that strong upper mantle velocity variations beneath ridge axis may be associated with the upwelling and partial melting within a lateral distance of 200 km from the axis [e.g., *Blackman et al.*, 1996]. Furthermore, data from the MELT experiment [*MELT Seismic Team*, 1998; *Evans et al.*, 1999; *Faul*, 2001] has suggested a partial melt zone several hundred kilometers wide beneath the southern EPR.

[39] The LVZ velocity of paths sampling the northern EPR and Galapagos ridge shows a mean value of 4.0–4.1 km s^{-1}, with no dependence on the path age (see Figure 15c). These velocities are consistent with an asthenosphere containing a small amount of partial melt [*Forsyth*, 1992], as was suggested by the large $|dVs/dT|$ value estimated from the lid velocities. The near-constant velocity values imply that if a more melt-rich zone exists beneath the axis, it is either too weak or too narrow to be observed within the resolution of our data set.

[40] The data from the southern EPR shows 3.8–4.0 km s^{-1} LVZ shear velocities, consistent with the presence of partial melt at these depths throughout the region. The LVZ velocities also exhibit a strong dependence on path age (see Figure 15c). This age dependence is probably not a reflection of plate cooling or the lack of vertical resolution in our models, as it is observed only for the southern EPR paths. Rather, it suggests that the melt distribution at 50–100 km depth beneath the southern EPR is concentrated near the ridge axis, and the concentration progressively weakens further away from the axis. It is difficult to judge whether the melt-rich zone is distributed along the entire length of the southern EPR [e.g., *Blackman et al.*, 1996; *Dunn and Forsyth*, 2003], or if it is concentrated west and north of the main MELT array [*Forsyth et al.*, 1998] instead. The geometry of this experiment is such that average age of each path correlates inversely with its propagation length along the southern EPR. Because of the overlap among paths that sample the southern EPR just north of the MELT array, their LVZ velocities could be produced by a localized mantle anomaly (see Figure 15a). This LVZ anomaly is also suggested by anomalous seafloor bathymetry in this region [*Cochran*, 1986]. The seafloor west of the EPR axis between 9°S and 22°S subsides with age at a slower rate than the plate to the east, suggesting the plate to the west is underlain by a hotter mantle. The fact that LVZ velocities correlate linearly with age suggests that the spatial averaging of a localized anomaly is an acceptable interpretation of our models.

[41] Our observation of a strong LVZ beneath the southern EPR is consistent with the earlier findings from the MELT experiment [e.g., *Webb and Forsyth*, 1998; *Dunn and Forsyth*, 2003]. Recent models obtained from 3-D surface and body wave inversions [*Shapiro and Ritzwoller*, 2002; *Gu et al.*, 2005] provide further support for a strong asthenospheric anomaly (Figure 16a), with lateral resolution on the order of 500 km, beneath the MELT array region of the southern EPR. For example, the isotropic shear velocities of *Gu et al.* [2005], obtained from radially anisotropic inversions of body and surface waves, favor a low-velocity anomaly at ~70 km depth that is absent in the northern EPR. The average LVZ velocities of our models (shown by line segments, Figure 16a) correlate with the distribution of fast (blue) velocities in the north and slow (red) velocities in the south. The paths that sample the southern EPR show lower average velocities than those traversing the northern EPR and Galapagos ridge. Figure 16b displays representative, well-resolved models of similar age (2–3 Myr) from each region. The events that illuminate the northern EPR and Galapagos ridge have compatible mantle structures with the LVZ of NF0-4. The southern EPR, however, shows a LVZ nearly 0.3 km/s slower than the aforementioned models. Differences in the width and symmetry of the partial melt zones could play a role: because the paths sampling the southern EPR are near zero age, they could be more affected by multipathing than those sampling the northern EPR and Galapagos spreading center. Still, the observed north-south difference is too large to be explained by geometry alone, differences in temperature, present-day

melting rate or past melt extraction between these regions should be important. Because of relatively weak constraint from *P* waves, hence the lack of a direct comparison between *P* and *S* at LVZ depths, it is difficult to distinguish between the effect of temperature, which would cause a high correlation between *P* and *S* wave speeds, and the effect of melting, which would preferentially reduce the speed and amplitude of shear waves. However, the two effects are not independent, in fact, considering the absolute velocity values (which are close to the solidus), it is most likely that partial melt is present under such a high-temperature environment.

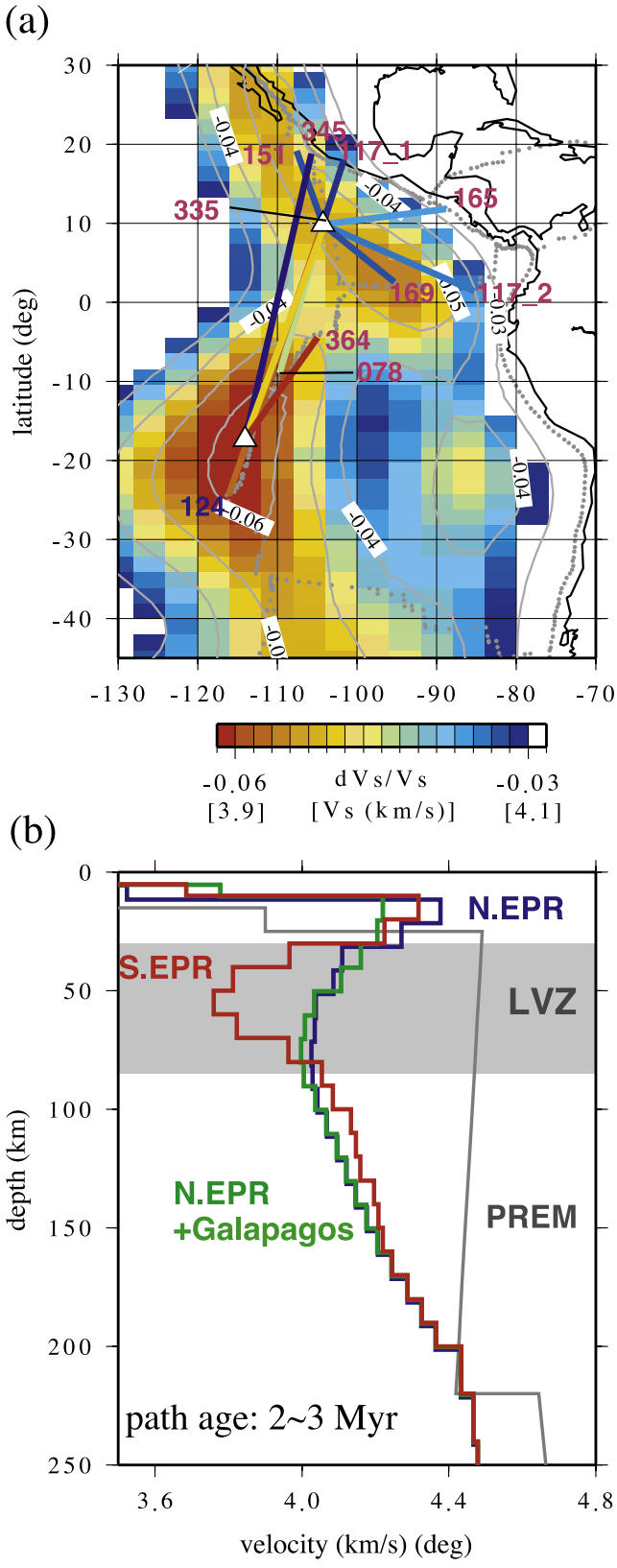

5. Implications and Conclusions

[42] This study provides new constraints on melting beneath the eastern Pacific ridge system. Our lid velocities are consistent with half-space cooling model of the oceanic lithosphere, with the thermal regime present in the northern EPR region being indistinguishable from that in the southern EPR (see Figure 15b).

[43] The substantial difference in the LVZ velocities between the north and south EPR could be partly accounted for a potential difference in upper mantle temperature. Recent models of the Superswell structure indicate that the excess temperature and melt need not produce a significant thermal perturbation to the lithosphere, which is consistent with the single thermal regime inferred from our lid models. An additional component is the possibility of a narrower melt zone beneath the northern ridge segments, such that it is invisible to the off-axis ray paths traversing the northern EPR. The remaining signal could be due to greater melt productivity via a process that does not produce a substantial temperature perturbation in the lithosphere, and/or, due to differences in melt extraction efficiency. If the structure under the southern EPR represents "normal" mantle beneath a fast spreading ridge, the mantle beneath the northern EPR must be considerably depleted in melt content. This could occur if the mechanism by which melt is extracted is (or has been in the past) more efficient under the northern EPR, thereby leaving less melt behind within the upper mantle [e.g., *Small and Danyushevsky*, 2003; *Lizarralde et al.*, 2004]. To first order, this suggestion is consistent with observations of crustal thickness in these two regions: the mean crustal thickness estimated for the ridge crest near 9°N (~6.7 km [*Canales et al.*, 2003]) is approximately 1 km larger than that found along the MELT array (~5.7 km [*Canales et al.*, 1998]). The geometry of the plates may play a key role: the Cocos plate combined with ridge spreading at both the EPR and Galapagos ridge may

Figure 16. (a) Background color map showing the isotropic shear velocities of *Gu et al.* [2005], obtained from global inversions of body and surface waves, at 70 km. The colors of the line segments show the average LVZ velocities from our models. The 3-D model contains a strong negative anomaly that is consistent with the slow, path-averaged shear velocities obtained by this study. (b) A model comparison for three typical events, all with average path ages of 2–3 Myr. The two events that sample the northern EPR and Galapagos ridge both contain a relatively mild LVZ, consistent with NF0-4. The southern EPR, however, shows a pronounced LVZ approximately 0.3 km/s slower than the others. The regional models of oceanic mantle are substantially slower than Voigt-averaged, isotropic PREM velocities in the top 250 km.

be more effective in removing the melt from the asthenospheric mantle, a scenario that is supported by a relatively deep ridge crest near the Galapagos triple junction [*Small and Danyushevsky*, 2003]. Conversely, if we consider the mantle beneath the northern EPR as "de facto" ridge mantle, then the southern EPR would require additional melt from other sources. One possible source is excess melting driven by the Pacific Superswell anomaly [e.g., *McNutt and Judge*, 1990], which has been invoked to explain the asymmetric bathymetry and seismic structure found in the MELT region [e.g., *MELT Seismic Team*, 1998]. The observed bathymetric asymmetry does not extend into the northern EPR, which would be consistent with the reduced melt content inferred from our northern EPR models. This hypothesis cannot explain the crustal thickness data, however; if extraction processes in both regions are comparable, then the greater melt production in the south should produce more crust [e.g., *Langmuir et al.*, 1992].

[44] The bottom of the LVZ is constrained to a depth of ~70 km to explain the long-period data from all of ridge segments examined by our study. This depth extent is consistent with petrologic models in which dry melting in upwelling mantle begins at a depth close to 70km. However, it is likely that we cannot resolve the presence of small amounts of melt that are produced deeper in the mantle at the wet solidus [e.g., *Hirth and Kohlstedt*, 1996].

[45] Finally, through waveform modeling, we were able to improve the depth constraints on the ocean transform (8 out of 10) earthquakes used in this study, using an effective amplitude analysis. Rather than adopting empirical depths from global inversions, or ones based on a priori assumptions about the crustal thickness beneath a path, we exploit the ratio between body and surface waves amplitudes at multiple stations. In spite of uncertainties associated with second-order effects such as Q and limited azimuthal coverage, our approach has shown some promise to determine more accurate earthquake depths using regional OBS recordings: for example, all of the events are relocated to shallower depths than 15 km (CMT), with five of them shallower or equal to 8 km and clearly above the Moho. Our depth estimates are similar to those associated with the 1992 Chain transform earthquakes by *Abercrombie and Ekström* [2001], but they are generally shallower than the event depths reported by the same study for the Romanche transform. On the basis of a crude temperature analysis the events examined here fit mostly within a 400–500°C isotherm. This is roughly consistent with previous estimates for transform fault earthquakes [*Bergman and Solomon*, 1988] but higher than previous estimates for intraplate earthquakes [*Wiens and Stein*, 1983].

[46] Several important issues related to the data set analyzed in this study should be explored in greater detail in the near future. One well-known issue is that wave speeds in mantle rocks are anisotropic, that is, shear wave velocities have strong dependencies on the direction of propagation and polarization. Although the majority of the data in this study can be modeled well using a simple isotropic waveform approach, issues related to the anisotropic (Love and Rayleigh) variation and nonspherical propagation effect of shear waves [*Ekström and Dziewonski*, 1998; *Levin et al.*, 1999; *Gaherty*, 2001; *Plomerova et al.*, 2002; *Gung et al.*, 2003; *Gu et al.*, 2005], especially those resulting from 3-D mantle structure beneath the axial rifts [*Wolfe and Solomon*, 1998; *Toomey et al.*, 2002; *Dunn and Forsyth*, 2003], are undoubtedly important issues that warrant future studies.

[47] **Acknowledgments.** We thank William Menke, Jack Xie, Won-Young Kim, and Shun Karato for helpful discussions during the preparation of this manuscript. We also thank Donald Forsyth, Doug Wiens, and Rob Dunn for constructive reviews and suggestions for improvement. Some of the figures were prepared using the GMT [*Wessel and Smith*, 1991] software. This is Lamont contribution 6742.

References

Abercrombie, R. E., and G. Ekström (2001), Earthquake slip on oceanic transform faults, *Nature*, *410*, 74–77.

Bassin, C., G. Laske, and G. Masters (2000), The current limits of resolution for surface wave tomography in North America, *Eos Trans. AGU*, *81*(48), Fall Meet. Suppl., Abstract S12A-03.

Bergman, E. A., and S. C. Solomon (1988), Transform fault earthquakes in the North Atlantic: Source mechanisms and depth of faulting, *J. Geophys. Res.*, *93*, 9027–9057.

Blackman, D. K., J.-M. Kendall, P. R. Dawson, H.-R. Wenk, D. Boyce, and J. Phipps Morgan (1996), Teleseismic imaging of subaxial flow at mid-ocean ridges: Travel time effects of anisotropic mineral texture in the mantle, *Geophys. J. Int.*, *127*, 415–426.

Canales, J. P., R. S. Detrick, S. Bazin, A. J. Harding, and J. A. Orcutt (1998), Off-axis crustal thickness across and along the East Pacific Rise within the MELT area, *Science*, *280*, 1218–1221.

Canales, J. P., R. S. Detrick, D. R. Tommey, and W. S. D. Wilcock (2003), Segment scale variations in the crustal structure of 150–300 kyr old fast spreading oceanic crust (East Pacific Rise, 8–15N 10–5N) from wide-angle seismic refraction profiles, *Geophys. J. Int.*, *152*, 766–794.

Cochran, J. R. (1986), Variations in subsidence rates among intermediate and fast spreading ridges, *Geophys. J. R. Astron. Soc.*, *87*, 421–454.

Dunn, R. A., and D. W. Forsyth (2003), Imaging the transition between the region of mantle melt generation and the crustal magma chamber beneath the southern East Pacific Rise with short-period Love waves, *J. Geophys. Res.*, *108*(B7), 2352, doi:10.1029/2002JB002217.

Dziewonski, A. M., and D. L. Anderson (1981), Preliminary reference Earth model, *Phys. Earth Planet. Inter.*, *25*, 297–356.

Ekström, G., and A. M. Dziewonski (1998), The unique anisotropy of the Pacific upper mantle, *Nature*, *394*, 168–172.

Evans, R. L., et al. (1999), Asymmetric electrical structure in the mantle beneath the East Pacific Rise at 17°S, *Science*, *286*, 752–756.

Faul, U. H. (2001), Melt retention and segregation beneath mid-ocean ridges, *Nature*, *410*, 920–923.

Forsyth, D. W. (1992), Geophysical constraints on mantle flow and melt generation beneath mid-ocean ridges, in *Mantle Flow and Melt Generation at Mid-Ocean Ridges*, *Geophys. Monogr. Ser.*, vol. 71, edited by J. Phipps Morgan, D. K. Blackman, and J. M. Sinton, pp. 1–65, AGU, Washington, D. C.

Forsyth, D. W., et al. (1998), Imaging the deep seismic structure beneath a mid-ocean ridge: The MELT experiment, *Science*, *280*, 1215–1218.

Fuchs, K., and G. Müller (1971), Computation of synthetic seismograms with the reflectivity method and comparison with observations, *Geophys. J. R. Astron. Soc.*, *23*, 417–433.

Gaherty, J. B. (2001), Seismic evidence for hot spot-induced buoyant flow beneath the Reykjanes Ridge, *Science*, *293*, 1645–1647.

Gu, Y. J., A. Lerner-Lam, A. M. Dziewonski, and G. Ekström (2005), Seismic evidence for deep anisotropy beneath the East Pacific Rise, *Earth. Planet. Sci. Lett.*, *232*, 259–272.

Gung, Y., M. Panning, and B. Romanowicz (2003), Global anisotropy and the thickness of continents, *Nature*, *422*, 707–711.

Herrmann, R. B., and C. Y. Wang (1985), A comparison of synthetic seismograms, *Bull. Seismol. Soc. Am.*, *75*, 41–56.

Hirth, G., and D. L. Kohlstedt (1996), Water in the oceanic upper mantle: Implications for rheology, melt extraction, and the evolution of the lithosphere, *Earth Planet. Sci. Lett.*, *144*, 93–108.

Jackson, I., M. S. Paterson, and J. D. Fitz Gerald (1992), Seismic wave dispersion and attenuation in Aheim dunite: An experimental study, *Geophys. J. Int.*, *108*, 517–534.

Jackson, I., J. D. Fitz Gerald, U. H. Faul, and B. H. Tan (2002), Grain-size-sensitive seismic wave attenuation in polycrystalline olivine, *J. Geophys. Res.*, *107*(B12), 2360, doi:10.1029/2001JB001225.

Karato, S. (1993), Importance of anelasticity in the interpretation of seismic tomography, *Geophys. Res. Lett.*, *20*, 1623–1626.

Karato, S. (1995), Effect of water on seismic wave velocities in the upper mantle, *Proc. Jpn. Acad., Ser. B*, *71*, 61–66.

Kato, M. (1997), An analysis of the temperature derivative of shear wave velocity in the oceanic lithosphere of the Pacific Basin, *J. Phys. Earth*, *45*, 67–71.

Kent, G. M., et al. (2000), Evidence from three dimensional seismic reflectivity images for enhanced melt supply beneath mid-ocean ridge discontinuities, *Nature*, *406*, 614–618.

Kido, M., and T. Seno (1994), Dynamic topography compared with residual depth anomalies in oceans and implications for age-depth curves, *Geophys. Res. Lett.*, *21*, 717–720.

Kind, R. (1978), The reflectivity method for a buried source, *J. Geophys.*, *44*, 603–612.

Klitgord, K. D., and J. Mammerickx (1982), Northern East Pacific Rise: Magnetic anomaly and bathymetric framework, *J. Geophys. Res.*, *87*, 6725–6750.

Langmuir, C. H., E. M. Klein, and T. Plank (1992), Petrological systematics of mid-ocean ridge basalts: Constraints on melt generation beneath ocean ridges, in *Mantle Flow and Melt Generation at Mid-Ocean Ridges*, *Geophys. Monogr. Ser.*, vol. 71, edited by J. Phipps Morgan, D. K. Blackman, and J. M. Sinton, pp. 183–280, AGU, Washington, D. C.

Levin, V., W. Menke, and J. Park (1999), Shear-wave splitting in Appalachians and Urals: A case for multilayered anisotropy, *J. Geophys. Res.*, *104*, 17,975–17,994.

Li, X.-D., and B. Romanowicz (1996), Comparison of global waveform inversions with and without considering cross-branch model coupling, *Geophys. J. Int.*, *121*, 695–709.

Lizarralde, D., J. B. Gaherty, J. A. Collins, G. Hirth, and S. Kim (2004), Spreading-rate dependence of melt extraction at mid-ocean ridges from far-offset seismic data, *Nature*, *432*, 744–747.

Lonsdale, P. (1985), Linear volcanoes along the Pacific-Cocos plate boundary, 9(N to the Galapagos triple junction, *Tectonophysics*, *116*, 255–279.

Lonsdale, P. (1995), Segmentation and disruption of the East Pacific Rise in the mouth of the Gulf of California, *Mar. Geophys. Res.*, *17*, 323–359.

Mammerickx, J., D. F. Naar, and R. L. Tyce (1988), The mathematician paleoplate, *J. Geophys. Res.*, *93*, 3025–3040.

McNutt, M. K., and A. V. Judge (1990), The superswell and mantle dynamics beneath the South Pacific, *Science*, *248*, 969–975.

MELT Seismic Team (1998), Imaging deep seismic structure beneath the mid-ocean ridge: The MELT experiment, *Science*, *280*, 1215–1218.

Montagner, J.-P. (2002), per mantle low anisotropy channels below the Pacific Plate, *Earth Planet. Sci. Lett.*, *202*, 263–274.

Mueller, R. D., W. R. Roest, J.-Y. Royer, L. M. Gahagan, and J. G. Sclater (1997), A digital age map of the ocean floor, *J. Geophys. Res.*, *102*, 3211–3214.

Nakanishi, I., and D. L. Anderson (1984), Aspherical heterogeneity of the mantle from phase velocities of mantle waves, *Nature*, *307*, 117–121.

Nishimura, C. E., and D. W. Forsyth (1989), The anisotropic structure of the upper mantle in the Pacific, *Geophys. J. R. Astron. Soc.*, *96*, 203–229.

Plomerova, J., V. Babuska, L. Vecsey, and D. Kouba (2002), Seismic anisotropy of the lithosphere around the Trans-European suture zone (TESZ) based on teleseismic body wave data of the TOR experiment, *Tectonophysics*, *360*, 89–114.

Randall, G. E. (1994), Efficient calculation of complete differential seismograms for laterally homogeneous Earth models, *Geophys. J. Int.*, *118*, 245–254.

Sato, H., I. S. Sacks, and T. Murase (1989), The use of laboratory velocity data for estimating temperature and partial melt fraction in the low-velocity zone: Comparison with heat flow and electrical conductivity studies, *J. Geophys. Res.*, *94*, 5689–5704.

Shapiro, N. M., and M. H. Ritzwoller (2002), Monte-Carlo inversion for a global shear-velocity model of the crust and upper mantle, *Geophys. J. Int.*, *151*, 88–105.

Small, C., and L. V. Danyushevsky (2003), Plate-kinematic explanation for mid-ocean-ridge depth discontinuities, *Geology*, *31*, 399–402.

Su, W.-J., R. L. Woodward, and A. M. Dziewonski (1994), Degree-12 model of shear velocity heterogeneity in the mantle, *J. Geophys. Res.*, *99*, 6945–6980.

Toomey, D. R., W. S. Wilcock, S. C. Solomon, W. C. Hammond, and J. A. Orcutt (1998), Mantle seismic structure beneath the MELT region of the East Pacific Rise from *P* and *S* wave tomography, *Science*, *280*, 1224–1227.

Toomey, D. R., W. S. Wilcock, J. A. Conder, D. W. Forsyth, J. D. Blundy, and E. M. Parmentier (2002), Asymmetric mantle dynamics in the MELT region of the East Pacific Rise, *Earth Planet. Sci. Lett.*, *200*, 287–295.

Turcotte, D. L., and E. R. Oxburgh (1967), Finite amplitude convective cells and continental drift, *J. Fluid Mech.*, *28*, 29–42.

Turcotte, D. L., and G. Schubert (1982), *Geodynamics Applications of Continuum Physics to Geological Problems*, 450 pp., John Wiley, Hoboken, N. J.

van der Lee, S. (2002), Deep below North America, *Science*, *294*, 1297–1298.

Webb, S. C., and D. W. Forsyth (1998), Structure of the upper mantle under the EPR from waveform inversion of regional events, *Science*, *280*, 1227–1229.

Weeraratne, D. S., D. W. Forsyth, and S. C. Webb (2003), Rayleigh wave tomography study of the oceanic upper mantle beneath intraplate volcanic chains west of the East Pacific Rise, *Eos Trans. AGU*, *84*(46), Fall Meet. Suppl., Abstract V12B-0581.

Wessel, P., and W. H. F. Smith (1991), Free software helps map and display data, *Eos Trans. AGU*, *72*(41), 445–446, 441.

Wiens, D. A., and S. Stein (1983), Age dependence of oceanic intraplate seismicity and implications for lithospheric evolution, *J. Geophys. Res.*, *88*, 6455–6468.

Wolfe, C. J., and S. C. Solomon (1998), Shear-wave splitting and implications for mantle flow beneath the MELT region of the East Pacific Rise, *Science*, *280*, 1230–1232.

Woodhouse, J. H., and A. M. Dziewonski (1984), Mapping the upper mantle: Three-dimensional modeling of Earth structure by inversion of seismic waveforms, *J. Geophys. Res.*, *89*, 5953–5986.

Xu, Y., and D. A. Wiens (1997), Upper mantle structure of the southwest Pacific from regional waveform inversion, *J. Geophys. Res.*, *102*, 27,439–27,451.

J. B. Gaherty, A. Lerner-Lam, and S. C. Webb, Lamont-Doherty Earth Observatory, Columbia University, 61 Route 9W, Palisades, NY 10964, USA.

Y. J. Gu, Department of Physics, University of Alberta, Edmonton, AB, T6G2J1, Canada. (jgu@phys.ualberta.ca)